516-34

N91-21078

p 29

# A PRESSURE BASED METHOD FOR THE SOLUTION OF VISCOUS INCOMPRESSIBLE TURBOMACHINERY FLOWS

G. V. Hobson*
and
B. Lakshminarayana

Department of Aerospace Engineering
Pennsylvania State University
University Park, PA 16803

PJ 304292
NAC-817
NSG-3266

## ABSTRACT

A new technique has been developed for the solution of the incompressible Navier-Stokes equations. The numerical technique, derived from a pressure substitution method (PSM), overcomes many of the deficiencies of the pressure correction method. This technique allows for the direct solution of the actual pressure in the form of a Poisson equation which is derived from the pressure weighted substitution of the full momentum equations into the continuity equation. Two-dimensional internal flows are computed with this method and the prediction of cascade performance is presented. The extension of the pressure correction method for the solution of three-dimensional flows is also presented.

## NOMENCLATURE

| | |
|---|---|
| $C_{\epsilon 1}, C_{\epsilon 2}, C_{\mu}$ | coefficients in turbulence model |
| $C_p$ | specific heat at constant pressure |
| $E$ | turbulent constant dependent on wall roughness |
| $f_1, f_2, f_{\mu}$ | low-Reynolds number turbulence model coefficients |
| $G_1, G_2, G_3$ | contravariant velocities |
| $h$ | static enthalpy |
| $H_1, H_2, H_3$ | transformation metrics |
| $J_{\xi}, J_{\eta}, J_{\zeta}$ | flux vectors |
| $\mathbb{J}$ | Jacobian of the transformation |
| $k$ | turbulent kinetic energy |
| $L$ | turbulent length scale |
| $p$ | static pressure |
| $Pr_t$ | turbulent Prandtl number |
| $Re$ | Reynolds number |
| $Re_t$ | turbulent Reynolds number, $\rho k^2/\mu\epsilon$ |

---

* Presently; Turbopropulsion Laboratory
Naval Postgraduate School
Monterey, CA 93943

| | |
|---|---|
| $Re_y$ | turbulent Reynolds number, $\rho y\sqrt{k}/\mu$ |
| $S^\phi$ | source term (for variable $\phi$) |
| $T$ | static temperature |
| $T'$ | fluctuating temperature |
| $Tu$ | turbulence intensity, $\sqrt{(\overline{u'^2})}\,/U_i$ |
| $u_i$ | mean velocity in direction $x_i$, $(u_1,u_2,u_3) \equiv (u,v,w)$ |
| $u'_i$ | fluctuating velocity in direction $x_i$ |
| $U_i$ | inlet total velocity |
| $x_i$ | Cartesian coordinate, $(x_1,x_2,x_3) \equiv (x,y,z)$ |
| $y^+$ | non-dimensionalized normal distance, $y\sqrt{(\tau_w/\rho)}/\nu$ |
| $\alpha,\beta,\gamma$ | transformation metrics |
| $\delta_{ij}$ | Kronecker delta |
| $\epsilon$ | dissipation rate of turbulent kinetic energy |
| $\kappa$ | von Karman constant, 0.42 |
| $\mu$ | molecular viscosity |
| $\mu_{eff}$ | effective viscosity, $\mu + \mu_t$ |
| $\mu_t$ | turbulent viscosity |
| $\nu$ | kinematic viscosity |
| $\Phi$ | dissipation function |
| $\phi$ | scalar variable |
| $\phi'$ | fluctuating dissipation |
| $\rho$ | density of fluid |
| $\Gamma^\phi$ | effective diffusion coefficient (for variable $\phi$) |
| $\sigma_k, \sigma_\epsilon$ | coefficients in turbulence model |
| $\tau_w$ | shear stress on the wall |
| $\xi,\eta,\varsigma$ | transformed coordinates |
| $\Delta\xi,\Delta\eta,\Delta\varsigma$ | computational domain grid spacing |
| $\omega_p$ | relaxation parameter for pressure equation |
| $\omega_u,\omega_v,\omega_w$ | relaxation parameter for momentum equations |

## Subscripts

| | |
|---|---|
| 0 | central grid point in finite difference molecule |
| d | downstream face of control volume |
| D | downstream grid point |
| e | east face of control volume |
| E | east grid point |
| i,j,k | tensor indices |
| i | inlet flow conditions |

| | |
|---|---|
| n | north face of control volume |
| N | north grid point |
| o | outlet flow conditions |
| P | first grid point away from the wall |
| s | south face of control volume |
| S | south grid point |
| u | upstream face of control volume |
| U | upstream grid point |

## INTRODUCTION

Turbomachinery flows are amongst the most complex encountered in engineering. These flows are three dimensional and highly turbulent and may include heat transfer. Unsteadiness and compressibility in turbomachinery flows are also relevant but will not be considered in this paper. Higher order turbulence models are also needed to resolve the transitional and near wall flow phenomena, which are important for loss and heat transfer predictions. Flow separation should also be accurately predicted with such models as these regions are inevitably present in modern highly loaded turbine and compressor blade rows.

This paper is mainly concerned with the development of a more efficient pressure based method and its application to turbomachinery incompressible flows.

A brief review of the relevant works follows. Hah (ref. 1) solved the uncoupled equations on a staggered grid. Higher order discretization was used for the convection terms to reduce numerical diffusion. The quadratic upsteam (QUICK) differencing by Leonard (ref. 2) and skew upwinding scheme by Raithby (ref. 3) were extended and modified. An algebraic Reynolds stress model modified for the effect of streamline curvature and rotation was used for the closure of the governing equations. Comparison with experimental data for an end-wall turbine cascade flow, showed that various complex three-dimensional viscous flow phenomena were well predicted.

An excellent review paper by Patankar (ref. 4) puts the treatment of convection and diffusion into perpective. He refers to a study done by Patel and Markatos (ref. 5) who evaluated eight different discretization schemes to solve the two-dimensional convection-diffusion equations. "They found that QUICK and its variants gave accurate and cost effective solutions when they converged. However they failed to converge for high flow rates and coarse grids." The situation becomes more acute for supersonic flows for which Patel et al. (ref. 6) concluded that the upwind scheme is the best choice.

Patankar (ref. 4) observes, "Thus, we have gone around full circle. Lower-order schemes such as upwind are stable and monotonic but lead to false diffusion. Higher-order schemes such as QUICK eliminate false diffusion but produce wiggles and often fail to converge. The search for the perfect method is still not over."

Rhie and Chow (ref. 7) presented a solution of the Navier-Stokes equations in general curvilinear coordinates on a non-staggered grid. A specific algorithm based on pressure weighting (PWM) was developed to suppress the pressure oscillations. This development was a major breakthrough for the solution of the fluid flow equations in generalised coordinates. They used the pressure correction method (PCM) to couple the momentum and continuity equations. The standard form of the k-$\epsilon$ model was used to describe the turbulence for flows over airfoils with and without trailing edge separation.

Recently, Rhie (ref. 8), extended his scheme to employ the pressure implicit split operator (PISO) concept with a multigrid procedure to enhance convergence. Within the several levels of pressure correction, the density was treated implicitly for the correction of the mass flow imbalance. This treatment was applicable for compressible flows. The method was tested for a wide range of flows, including three-dimensional driven cavity and a turbine end-wall cascade.

Three different formulations for non-staggered grids have been suggested by Shih and Ren (ref. 9). Some employ the Poisson equation for pressure, in place of the continuity equation. All of the algorithms, proposed by them, solve for the pressure directly and not the pressure correction as in the SIMPLE algorithm. When the continuity equation is used, a Pressure Substitution Method (PSM) is employed. However the equations were solved in non-conservative form, thus resulting in a purely finite difference method.

Hobson and Lakshminarayana (ref. 10) presented a control volume formulation of the pressure substitution method for the solution of the Navier-Stokes equations describing incompressible flows. The application of this method to two-dimensional cascade flows is presented. The Low-Reynolds number k-$\epsilon$ turbulence model according to Lam and Bremhorst (ref. 11) is used to resolve the turbulence within the flow.

Three-dimensional flows are calculated with the pressure correction method similar to that used by Rhie (ref. 12) and the standard High-Reynolds number k-$\epsilon$ turbulence model including wall functions is used. The computation of turbulent flow in a turbine end-wall cascade is presented.

## THEORETICAL FORMULATION

### The Incompressible Viscous Flow Equations

For steady-mean incompressible flow, the time-averaged continuity equation and the Reynolds averaged Navier-Stokes equation can be written in Cartesian tensor form:

$$\frac{\partial(\rho u_i)}{\partial x_i} = 0 \qquad [1]$$

$$\frac{\partial(\rho u_i u_j)}{\partial x_j} = - \frac{\partial p}{\partial x_j} + \frac{\partial}{\partial x_j}\left\{\mu\left[\frac{\partial u_j}{\partial x_i} + \frac{\partial u_i}{\partial x_j}\right] - \rho\overline{u_i' u_j'}\right\} \qquad [2]$$

where $\rho$ is the mean density, $u_j$ the mean velocity, p the mean pressure and $\mu$ the molecular viscosity. The instantaneous velocity, $u'_i$, with an overbar "—" implies a time averaged quantity.

For the prediction of heat transfer in non-isothermal flows through turbines, the incompressible energy equation is also solved. The form used is given as follows,

$$\frac{\partial(\rho u_i h)}{\partial x_j} = \frac{\partial}{\partial x_j}\left\{\Gamma^T \frac{\partial T}{\partial x_i} - \rho\overline{u'_i h'}\right\} + \mu(\Phi + \overline{\phi'}) \qquad [3]$$

where h is the static enthalpy, $\Gamma^T$ the thermal conductivity of the gas, T the static temperature. Once again, the averaged fluctuating correlations are present, which will be described in the next section. The dissipation function, $\Phi$, is

$$\Phi = \left[\frac{\partial u_j}{\partial x_i} + \frac{\partial u_i}{\partial x_j}\right]\frac{\partial u_j}{\partial x_i} \qquad [4]$$

Assuming that the specific heat, $C_p$, is constant and the gas is ideal, the static enthalpy is replaced by the static temperature, according to the following relationship.

$$h = C_p T \qquad [5]$$

## Two-Equation Low-Reynolds Number Turbulence Model

To solve equations [2] and [3], one must specify the Reynolds shear stress, $\rho\overline{u'_i u'_j}$, and heat flux, $\rho\overline{u'_i T'}$. A turbulent or "eddy" viscosity, $\mu_t$, and a turbulent Prandtl number, $Pr_t$, are defined according to the Boussinesq approximation (ref. 13) such that,

$$-\rho\overline{u'_i u'_j} = \mu_t\left[\frac{\partial u_j}{\partial x_i} + \frac{\partial u_i}{\partial x_j}\right] - \frac{2}{3}k\delta_{ij} \qquad [6]$$

$$-\rho\overline{u'_i T'} = \frac{\mu_t}{Pr_t}\left[\frac{\partial T}{\partial x_i}\right] \qquad [7]$$

where $\delta_{ij}$ is the Kronecker delta and k is the turbulent kinetic energy.

The isotropic eddy viscosity model was used to obtain an effective viscosity, $\mu_{eff}$, which is the sum of the turbulent viscosity and molecular viscosity.

For the purpose of this paper, the turbulent Prandtl number will be assumed constant and equal to 0.9. Although this is not generally true, it has been found to be a reasonably good approximation for most boundary layer flows with mild temperature gradients. The role of the turbulence model now becomes that of determining the correct value of $\mu_t$.

From the k-$\epsilon$ turbulence model, as proposed by Launder and Spalding (ref. 14), the turbulent eddy viscosity $\mu_t$ is given by,

$$\mu_t = f_\mu C_\mu \rho \frac{k^2}{\epsilon} \qquad [8]$$

where k is the turbulent kinetic energy and $\epsilon$ is the turbulent energy dissipation and each are defined as follows,

$$k = \frac{1}{2}\overline{u_i' u_i'} \qquad [9]$$

$$\epsilon = \frac{\mu}{\rho}\overline{\frac{\partial u_i'}{\partial x_j}\frac{\partial u_i'}{\partial x_j}} \qquad [10]$$

The modelled equations for the transport of k and $\epsilon$ are given as follows,

$$\frac{\partial(\rho u_i k)}{\partial x_j} = \frac{\partial}{\partial x_j}\left[\frac{\mu_t}{\sigma_k}\frac{\partial k}{\partial x_j}\right] + \mu_t\left[\frac{\partial u_j}{\partial x_i} + \frac{\partial u_i}{\partial x_j}\right]\frac{\partial u_j}{\partial x_i} - \epsilon \qquad [11]$$

$$\frac{\partial(\rho u_i \epsilon)}{\partial x_j} = \frac{\partial}{\partial x_j}\left[\frac{\mu_t}{\sigma_\epsilon}\frac{\partial \epsilon}{\partial x_j}\right] + f_1 C_{\epsilon 1}\mu_t \frac{\epsilon}{k}\left[\frac{\partial u_j}{\partial x_i} + \frac{\partial u_i}{\partial x_j}\right]\frac{\partial u_j}{\partial x_i} - f_2 C_{\epsilon 2}\frac{\epsilon^2}{k} \qquad [12]$$

Upon consideration of equations [8], [11] and [12], one can see that there are five empirical constants; $C_\mu$, $C_{\epsilon 1}$, $C_{\epsilon 2}$, $\sigma_k$, $\sigma_\epsilon$, and three empirical functions; $f_\mu$, $f_1$, and $f_2$. The values, of the five constants, used in this paper are those suggested as "standard" by Launder and Spalding (ref. 14). These assume the following values,

$$C_\mu=0.09,\ C_{\epsilon 1}=1.44,\ C_{\epsilon 2}=1.92,\ \sigma_k=1.0,\ \sigma_\epsilon=1.3 \qquad [13]$$

Turbulent motions immediately adjacent to the wall are significantly influenced by the presence of the wall. Here the magnitude of the effective turbulent viscosity becomes small, and the effects of the molecular viscosity become important. Experimental work has shown that in some turbulent flow situations, there exists a common structure or behavior near the wall. Under these conditions both the mean velocities and the measurable turbulence quantities exhibit nearly universal behavior. The knowledge of this structure has allowed the formulation and use of the so-called wall-functions. These functions algebraically bridge the near wall region and eliminate the need for more expensive and time consuming calculations with a fine grid near the wall.

Unfortunately, there are many flow situations of interest where this near-wall similarity breaks down. Large pressure gradients are found in the leading edge and trailing edge regions of turbomachinery blade profiles due to the high streamline curvature in these areas. This, and mass transfer at the wall, for example, both alter the near-wall flow, thus wall functions cannot be used. To incorporate these effects into the turbulence models, a variety of suggestions have been made. The purpose of the functions $f_\mu$, $f_1$ and $f_2$ is to provide a similar modification to the k-$\epsilon$ model, thus extending the validity of the equations through the viscous sub-layer to the wall. Use is made of two "turbulent Reynolds numbers." These are defined as follows,

$$Re_t = \frac{\rho k^2}{\mu \epsilon} \qquad [14]$$

$$Re_y = \frac{\rho y \sqrt{k}}{\mu} \qquad [15]$$

Patel et al. (ref. 15) give a good description of these functions.

The three functions given by Lam and Bremhorst (ref. 11) are as follows:

$$f_\mu = \left[1.0 - \exp^{(-0.0165 Re_y)}\right]^2 \left[1.0 + \frac{20.5}{Re_t}\right] \qquad [16]$$

$$f_1 = 1.0 + \left[\frac{0.05}{f_\mu}\right]^3 \qquad [17]$$

$$f_2 = 1.0 - \exp(-Re_t^2) \qquad [18]$$

This turbulence model has been chosen for use in this paper for a number of reasons. First, it has been used, by Rodi and Scheuerer (ref. 16), to predict transitional flow over a turbine blade with a boundary layer code. Second, when compared to other LRN k-$\epsilon$ models it has been shown by Patel et al. (ref. 15) to be amongst the best in predicting the characteristics of fully turbulent flow. Third it has very simple boundary conditions and in general the model is clean and straightforward to code.

## Transformation of the Basic Equations

The continuity equation [1] can be expanded to give,

$$\frac{\partial(\rho u)}{\partial x} + \frac{\partial(\rho v)}{\partial y} + \frac{\partial(\rho w)}{\partial z} = 0 \qquad [19]$$

The set of conservation equations describing the transport of momentum [2] can be written in Cartesian coordinates for a scalar variable as,

$$\frac{\partial(\rho u\phi)}{\partial x} + \frac{\partial(\rho v\phi)}{\partial y} + \frac{\partial(\rho w\phi)}{\partial z} = \frac{\partial}{\partial x}\left[\Gamma^{\phi}\frac{\partial\phi}{\partial x}\right] + \frac{\partial}{\partial y}\left[\Gamma^{\phi}\frac{\partial\phi}{\partial y}\right] + \frac{\partial}{\partial z}\left[\Gamma^{\phi}\frac{\partial\phi}{\partial z}\right] + S^{\phi} \qquad [20]$$

where $\Gamma^{\phi}$ is an effective diffusion coefficient and $S^{\phi}$ denotes the source term. For the momentum equations the source term is a function of the pressure gradient. When new independent variables $\xi,\eta$ and $\varsigma$ are introduced, Eq. [19] and [20] changes according to the following transformation $\xi=\xi(x,y,z)$, $\eta=\eta(x,y,z)$ and $\varsigma=\varsigma(x,y,z)$ as represented in Fig. 1.

The transformation of partial derivatives is presented in the Appendix. Upon substitution and after some manipulation the basic equations [19] and [20] are transformed into the following form.

$$\frac{\partial(\rho G_1)}{\partial\xi} + \frac{\partial(\rho G_2)}{\partial\eta} + \frac{\partial(\rho G_3)}{\partial\varsigma} = 0 \qquad [21]$$

$$\frac{\partial(\rho G_1\phi)}{\partial\xi} + \frac{\partial(\rho G_2\phi)}{\partial\eta} + \frac{\partial(\rho G_3\phi)}{\partial\varsigma} = \frac{\partial}{\partial\xi}\left\{\Gamma^{\phi}\left[\alpha\frac{\partial\phi}{\partial\xi} + H_1\frac{\partial\phi}{\partial\eta} + H_2\frac{\partial\phi}{\partial\varsigma}\right]\right\} +$$

$$\frac{\partial}{\partial\eta}\left\{\Gamma^{\phi}\left[H_1\frac{\partial\phi}{\partial\xi} + \beta\frac{\partial\phi}{\partial\eta} + H_3\frac{\partial\phi}{\partial\varsigma}\right]\right\} + \frac{\partial}{\partial\varsigma}\left\{\Gamma^{\phi}\left[H_2\frac{\partial\phi}{\partial\xi} + H_3\frac{\partial\phi}{\partial\eta} + \gamma\frac{\partial\phi}{\partial\varsigma}\right]\right\} + S^{\phi} \qquad [22]$$

## Vector Form of the Basic Equations

Only the source term $S^{\phi}$ takes on a different form for the three different directions. These are,

$$(1)\ \phi = u;\quad S^{\phi} = -\frac{\partial p}{\partial x} = -\xi_x\frac{\partial p}{\partial\xi} - \eta_x\frac{\partial p}{\partial\eta} - \varsigma_x\frac{\partial p}{\partial\varsigma}$$

$$(2)\ \phi = v;\quad S^{\phi} = -\frac{\partial p}{\partial y} = -\xi_y\frac{\partial p}{\partial\xi} - \eta_y\frac{\partial p}{\partial\eta} - \varsigma_y\frac{\partial p}{\partial\varsigma} \qquad [23]$$

$$(3)\ \phi = w;\quad S^{\phi} = -\frac{\partial p}{\partial z} = -\xi_z\frac{\partial p}{\partial\xi} - \eta_z\frac{\partial p}{\partial\eta} - \varsigma_z\frac{\partial p}{\partial\varsigma}$$

The source terms for the scalar equations considered such as the energy, turbulent kinetic energy and dissipation equations are mainly of scalar form.

## Discretization of the Transport Equations

The conservative form of the equation is derived for numerical computation, the integral form of the continuity equations [21] over the control volume, as shown in Fig. 2, is obtained as follows,

$$\int_u^d\int_s^n (\rho G_1)_w^e d\eta d\varsigma + \int_u^d\int_w^e (\rho G_2)_s^n d\xi d\varsigma + \int_s^n\int_w^e ( \rho G_3)_u^d d\xi d\eta = 0 \qquad [24]$$

and the transport equation [22] is,

$$\int_u^d\int_s^n (\rho G_1\phi)_w^e d\eta d\varsigma + \int_u^d\int_w^e (\rho G_2\phi)_s^n d\xi d\varsigma + \int_s^n\int_w^e (\rho G_3\phi)_u^d d\xi d\eta =$$

$$\int_u^d\int_s^n \left\{\Gamma^\phi\left(\alpha\frac{\partial\phi}{\partial\xi} + H_1\frac{\partial\phi}{\partial\eta} + H_2\frac{\partial\phi}{\partial\varsigma}\right)\right\}_w^e d\eta d\varsigma \quad +$$

$$\int_u^d\int_w^e \left\{\Gamma^\phi\left(H_1\frac{\partial\phi}{\partial\xi} + \beta\frac{\partial\phi}{\partial\eta} + H_3\frac{\partial\phi}{\partial\varsigma}\right)\right\}_s^n d\xi d\varsigma \quad +$$

$$\int_s^n\int_w^e \left\{\Gamma^\phi\left(H_2\frac{\partial\phi}{\partial\xi} + H_3\frac{\partial\phi}{\partial\eta} + \gamma\frac{\partial\phi}{\partial\varsigma}\right)\right\}_u^d d\xi d\eta \quad +$$

$$\int_u^d\int_s^n\int_w^e S^\phi \; d\xi d\eta d\varsigma \qquad [25]$$

where n, s, e, w, u and d are the locations of the intersection between the control volume faces and the grid lines.

Equations [24] and [25] can be rearranged as follows:

$$(\rho G_1\Delta\eta\Delta\varsigma)_w^e + (\rho G_2\Delta\xi\Delta\varsigma)_s^n + (\rho G_3\Delta\xi\Delta\eta)_u^d = 0 \qquad [26]$$

and,

$$(J_\xi\Delta\eta\Delta\varsigma)_w^e + (J_\eta\Delta\xi\Delta\varsigma)_s^n + (J_\varsigma\Delta\xi\Delta\eta)_u^d =$$

$$\left\{\Gamma^\phi\left(H_1\frac{\partial\phi}{\partial\eta} + H_2\frac{\partial\phi}{\partial\varsigma}\right)\Delta\eta\Delta\varsigma\right\}_w^e \quad +$$

$$\left\{\Gamma^\phi\left(H_1\frac{\partial\phi}{\partial\xi} + H_3\frac{\partial\phi}{\partial\varsigma}\right)\Delta\xi\Delta\varsigma\right\}_s^n \quad +$$

$$\left\{\Gamma^\phi\left(H_1\frac{\partial\phi}{\partial\xi} + H_3\frac{\partial\phi}{\partial\eta}\right)\Delta\xi\Delta\eta\right\}_u^d \quad + \quad S^\phi\Delta\xi\Delta\eta\Delta\varsigma \qquad [27]$$

where,

$$J_\xi = \rho G_1 \phi - \Gamma^\phi \alpha \frac{\partial \phi}{\partial \xi}$$

$$J_\eta = \rho G_2 \phi - \Gamma^\phi \beta \frac{\partial \phi}{\partial \eta} \qquad [28]$$

$$J_\varsigma = \rho G_3 \phi - \Gamma^\phi \gamma \frac{\partial \phi}{\partial \varsigma}$$

which are the flux vectors through the faces of the control volume in Fig. 2.

The source term is assumed to be acting at the centre, and constant within the control volume.

The discretized form of the continuity equation [26] has been described in detail by Hobson and Lakshminarayana (ref. 10) for two-dimensional flows. Equation [27] is discretized by using central differencing and linear interpolation in the computational domain. The coefficients of the resulting difference equation are modified according to the hybrid scheme of Spalding (ref. 17). For a cell Reynolds number less than or equal to two the hybrid scheme uses central differencing including both the convection and diffusion terms. As the cell Reynolds number exceeds two the hybrid scheme switches to upwind differencing with only the convective contribution; the diffusion terms are neglected.

## Boundary Conditions

No-slip boundary conditions are used for the velocities at a solid wall, where they are all set equal to zero. For cascade flows, periodic boundary conditions are implemented upstream and downstream of the blades on the periodically generated meshes. When solving along a periodic line in the blade-to-blade plane, two consequences result, which alter the tri-diagonal implicit matrix system of size N, which is usually used to solve between solid boundaries. First, an additional grid point is incorporated into the system, resulting in an N+1 system of simultaneous equations. Second, a cyclic tri-diagonal matrix system results, which is solved with the algorithm presented by Napolitano (ref. 18).

The inlet flow velocities are specified and fully developed flow is assumed to exist at the exit plane. The exit plane has to be situated far enough downstream of the blade row, where the assumption that the streamwise gradients are small is valid.

For the pressure substitution method the boundary condition required to solve the pressure equation is that the normal derivative of the pressure vanishes at solid boundaries, which is a reasonable assumption for high Reynolds number.

The boundary condition required to solve the pressure correction equation is that the normal derivative of the pressure correction, p', vanishes at the boundary in the computational domain. The actual pressure value at the boundary is determined by extrapolation from the interior nodes to the wall with the condition of zero normal derivative of the pressure.

Since Neumann boundary conditions are used for either the pressure correction method or the pressure substitution method, the pressure must be kept constant at one grid point. This control point is usually taken to be one of the inlet grid points, where the pressure gradients are small.

For the solution of the energy equation to predict the variation of heat transfer coefficients over turbine blades, the blade wall temperature is specified from experimental results.

The inlet turbulent kinetic energy and dissipation rate is determined by specifying an inlet turbulence intensity, Tu, and length scale, $L_i$, associated with the inlet flow. Most sets of experimental data have the turbulence intensity quoted, however the length scale has to be determined from the physical dimensions of the turbulence generator. In most cascade tests, grids are used upstream of the cascade, to generate the required turbulence levels. The length scale is of the order of the characteristic dimension of the rods that make up the grid. The inlet turbulent kinetic energy is thus determined from the following,

$$k_i = \frac{3}{2}(\mathrm{Tu}\ U_i)^2 \qquad [29]$$

where $U_i$ is the inlet total velocity. The inlet dissipation rate is then determined from the following,

$$\epsilon_i = \frac{k^{\frac{3}{2}}}{L_i} \qquad [30]$$

The boundary condition at the wall for the turbulent kinetic energy, k, takes on two definitions. For the "standard" form of the equations, with wall functions, the following condition is applied.

$$\left.\frac{\partial k}{\partial y}\right|_{\mathrm{wall}} = 0 \qquad [31]$$

The value of k is set equal to zero at the wall in the LRN model.

The idea behind the wall function method is that the turbulent length scale increases linearly, with distance from the wall beyond the viscous sublayer. The fluxes of momentum to the wall are then supposed, if the first grid point is in the fully turbulent region, to obey the relation,

$$\frac{u_p}{(\tau/\rho)_w} C_\mu^{1/4} k^{1/2} = \frac{1}{\kappa} \ln\left[\rho E y_p \frac{(C_\mu^{1/2} k_p)^{1/2}}{\mu}\right] \qquad [32]$$

Here $u_p$, $\tau_w$, and $y_p$ are, respectively, the time-averaged velocity of the fluid at the first grid point P away from the wall, the shear stress on the wall in the direction of the velocity $u_p$ and the distance of the point P from the wall. E is a constant and is a function of the wall roughness, approximately equal to 9.0 for a smooth wall, and $\kappa$ (=0.42) is the von Karman constant.

When calculating $k_p$, it is necessary to assign a value for the average energy-dissipation rate over the control volume, this is to be deduced from the assumption that,

$$\int_0^{y_p} \epsilon \, dy = C_\mu \frac{k_p^{3/2}}{\kappa} \ln\left[\frac{\rho E y_p (C_\mu^{1/2} k_p)^{1/2}}{\mu}\right] \qquad [33]$$

The appearance of this logarithmic function results from the necessity to presume that,

$$\epsilon_p = \frac{(C_\mu^{1/2} k_p)^{3/2}}{\kappa y_p} \qquad [34]$$

which is the boundary condition used for the dissipation rate of turbulent kinetic energy.

For the LRN model the boundary condition for the dissipation equation is,

$$\frac{\partial \epsilon}{\partial y} = 0 \qquad [35]$$

It is clear that the boundary conditions for the low-Reynolds number model are simpler than wall functions, particularly in their implementation into a computer code. Because of the requirement that the viscous sublayer be adequately resolved, the LRN was used only for two-dimensional flows. Wall functions were used for the three-dimensional flow test cases as a result of limited computer memory.

## Solution Algorithm and Relaxation Technique

The pressure substitution method (PSM) is used for the solution of two-dimensional flows and is fully described in reference 10. Upstream and downstream of the cascade the periodic solver according to Napolitano (ref. 20) is used and between the blade surfaces a tri-diagonal matrix solver is used for the successive line under-relaxation (SLUR) of the computational domain. Implicit solution is in the cross-stream direction and the line sweeps are performed in the streamwise direction.

The three-dimensional calculations were carried out with the pressure correction method. This algorithm is fully described by Rhie (ref. 12) and is a logical extension of the two-dimensional form as described in reference 7. The alternating direction implicit (ADI) method with the implicit periodic solver is used to calculate the three-dimensional flow through an end wall cascade.

The alternating direction implicit (ADI) method will be described by refering to Fig. 3. SLUR proceeds by taking all lines in the same direction in a repetitive manner. The convergence rate can be improved by following the sequence by rows, say, by a second sequence in the column direction. Such sequencing was used in the cross-stream plane for the cascade flows and this planar solution was advanced in the streamwise direction.

If there are I=1,NI grid points in the blade-to-blade direction and J=1,NJ grid points in the spanwise direction, as shown in Fig. 3, then on a cross-stream plane between the blades the ADI solution is performed from grid points 2 to NI-1 and 2 to NJ-1. However upstream (from grid points K=2 to KSTART) and downstream (from K=KFINIT to NK-1) of the cascade, as mentioned earlier, an additional periodic grid point is included in the blade-to-blade surface. Thus for the ADI line sweep in the blade-to-blade direction the periodic solver is used between grid points 1 and NI-1 (the values at NI then being set equal to those at 1). During the second ADI sweep in the spanwise direction, an additional line relaxation is performed on the periodic line, at I=1, from J=2 to NJ. Once again, to ensure periodicity the values at I=NI along the line J=2,NJ-1 are set equal to those at I=1. This completes an ADI sweep in the cross plane of the computational domain representing a cascade geometry. The solution is now advanced in the streamwise, or K, direction.

As the periodic solver is an extension of the Thomas algorithm (ref. 19), this solution procedure is believed to be consistent. The experience gained with the periodic solver in the solution of two-dimensional flows, showed that periodic solutions are efficiently achieved in an implicit manner, and thus was readily extended to three-dimensional flows.

## RESULTS AND DISCUSSION

### Laminar Flow in a Cascade

The test case is that of flow through a cascade of symmetrical NACA 0012 airfoils, which Rosenfeld and Wolfshtein (ref. 20) also computed. A comparison between the convergence histories of the pressure correction method (PCM) and the new pressure substitution method (PSM) was conducted for this configuration.

The cascade had a solidity, or pitch-to-chord ratio, of 1.0, and the airfoils had a stagger angle of 30 degrees. The Reynolds number, based on chord length, of the inlet total velocity was 1000. The incidence angle was varied between -10 and 15 degrees. They used 81x37 grid points with a computational "O" type grid. Their formulation was based on the vorticity and stream function equations.

The present computations were performed on a "H" type grid with 57x51 grid points. Almost the same number of grid points were used for the two studies, however the "O" grid used by Rosenfeld and Wolfshtein (ref. 20) gives more grid points on the airfoil surface that the present "H" grid. The comparison between the PSM and PCM algorithms were performed at various relaxation parameters for the momentum equations.

Fig. 4 shows the comparison of the convergence rate for the highest relaxation parameters ($\omega_u = \omega_v = 0.8$, and $\omega_p = 1.0$). The PSM shows a significant improvement over the PCM which seems to indicate that at least the initial stages of convergence of the PSM is more favorably affected by the relaxation parameter than the PCM. The above test case was compared with zero degrees inlet incidence angle. A comparison of the predicted static pressure coefficient over the airfoil with that computed by Rosenfeld and Wolfshtein (ref. 20) is presented in Fig. 5. The absolute levels of pressure coefficient do not compare well. However, the predicted negative lift coefficient ($C_L = -0.0310$) is within 4% of that predicted by Rosenfeld and Wolfshtein (ref. 20) who predicted $C_L = 0.0322$. The negative lift force created at this incidence angle causes a negative turning angle of -0.7 degrees through the cascade. The predictions using the PSM and PCM resulted in plots on the same curve.

An additional test case was computed with the PSM to predict the flow at the -10 degrees incidence case. The comparison with the predicted pressure coefficient as computed by Rosenfeld and Wolfshtein (ref. 20) is shown in Fig. 6. This comparison is better than the zero degree incidence test case, and the predicted $C_L = -0.389$ compares within 3% of their prediction of $C_L = -0.39711$. The present method does not suffer from pressure field oscillations around the trailing edge.

## Turbulent Flow Through a Cascade of Double Circular Arc Profiles with Flow Detachment

For the test case of turbulent flow through a cascade, the predictions made by the present method were compared with the experimental data obtained by Zierke and Deutsch (ref. 21). The blade section was a double circular arc, The computed test case was for the near design case of -1.5 degrees incidence.

The modified version of the GRAPE code was used to generate the H-grid which extended half a chord upstream and one and a half chords downstream of the blade. The inlet angle of the grid was aligned with the incoming flow at 51.5 degrees and the outlet grid angle was set equal to the measured outlet flow angle of 2.1 degrees. The Navier-Stokes calculations were on a 130 streamwise by 100 tangential computational grid as shown in Fig. 7. The residuals were reduced by four orders of magnitude in roughly 2000 iterations. This corresponded to 20 minutes on the ETA-10 supercomputer, only using the optimization capabilities of the compiler which vectorizes inner DO-loops. The slope of the convergence plots were not monotonic and flattened out after 300 iterations.

Fig. 8 shows a comparison of the calculated and measured static pressure distribution. The experimental measurements indicated a possible separation region near the trailing edge. Surface flow visualisation tests using the chemical sublimation method showed, with a 95% confidence level, a region of low shear stress at 45.1% ±2.3% chord.

The comparison of the blade surface skin friction distribution is presented in Fig. 9. Transition of the pressure surface boundary layer from laminar to turbulent flow is predicted by the technique. The onset of transition is predicted to be at 10% chord, which is early compared to the experimentally determined transition process. Transition seems to be complete by 30% chord, thus the length of the transitional region is in agreement with that determined experimentally. The experimental points were determined by fitting a spline through the measured boundary layer profiles. The level of skin friction coefficient in the fully turbulent region is accurately predicted, as well as the final increase at the trailing edge. Good agreement is achieved between the predicted and experimental skin friction coefficient on the suction surface of the blade. Shown on this figure is the separation point as determined by the flow visualisation technique and the separation point as predicted by the code with good agreement. The levels of skin friction are very close to zero over most of the rear part of the blade.

## Turbulent Flow Through a Cascade of Turbine Nozzles Including Heat Transfer

The computer program was used to compute turbine cascade flows for which Turner (ref. 22) conducted heat transfer measurments. A review of the literature showed that few incompressible flow experiments, including heat transfer measurements, have been documented. Turner (ref. 22) tested a nozzle blade section, as shown in Fig. 10, that was the same as the one used by Bayley and Turner (ref. 23) and Bayley and Wood (ref. 24). The blade chord was 70 mm and the aspect ratio and pitch-to-chord ratio were 1.34 and 0.65, respectively. The stagger angle was 40.6 degrees, and the inlet and outlet flow angles were 0.0 and 61.0 degrees, respectively. Three exit Mach numbers (0.75, 0.65, 0.55) were considered. At each Mach number tests were done at three turbulence intensities, namely 5.9%, 2.2% and 0.45%.

The cascade tunnel delivered 1.5 atmospheres of air, at 90 degrees C, to the test section. The blades were internally cooled with air at 20 degrees C, which produced a sufficient temperature gradient for heat transfer experiments. At the highest turbulence level the average gas-to-wall temperature difference was 28 degrees C and 40 degrees C at the lowest turbulence level. The exit Reynolds number based on the nozzle chord was $1.05 \times 10^6$.

Since the present predictions are valid for incompressible flow, only the low Mach number test case was considered. For this test case, the aerodynamic experimental test data were obtained from Bayley and Wood (ref. 24). Although porous blade sections were tested, they did present blade surface velocity distributions for the solid blades.

The turbulence of the flow at entry to the cascade was varied by placing various grids and drilled plates one chord distance upstream of the blade. Unfortunately, neither the diameter of the grids nor their character dimensions were quoted by Turner (ref. 22). The turbulence length scale, $L_i$, was thus set equal to the leading edge radius (0.26cm) of the nozzle blades for all the test cases considered. This value was used in equation [30] to determine the inlet levels of the dissipation rate $\epsilon$.

As shown in Fig. 10, a 100x132 computational H-grid was used with the normal grid spacing at the blade surface such that the first grid point was at a $y^+$ of 1.0. The inlet angle of the grid to the cascade was set equal to zero degrees, and the exit grid angle was set equal to 60 degrees.

The predicted velocity distribution over the blade surface is compared to the distribution calculated from the static pressure measurements in Fig. 11. The local velocity was derived by assuming isentropic expansion from the inlet total pressure to the static pressure, either measured or predicted, recorded on the blade surface. The sudden acceleration of the flow around the leading edge on the suction surface is captured, and the subsequent acceleration on the front section of the blade. The maximum velocity level is accurately predicted, and the diffusion process that results on the suction surface after the turbine throat is adequately resolved. The level of local velocity is slightly high on the rear section of the suction surface. The rapid diffusion process on the rear part of the suction surface results in flow separation which is predicted at the trailing edge. The continual flow acceleration process on the pressure surface is well predicted over its entire length.

Turner (ref. 22) showed that the mean heat transfer results for a turbine blade operating at one Reynolds number, but at different turbulence levels, vary substantially. At a Reynolds number of $1.0 \times 10^6$ the mean heat transfer coefficient varied from $8.5 \times 10^2$ to $1.05 \times 10^3$ for varying inlet turbulence intensity levels from 0.45 to 5.9% respectively. For different turbulence levels the slope of the Nusselt number versus Reynolds number also varied, the actual slopes are presented by Turner. A distinct increase in the blade surface temperature was measured. No data were presented on the cooling system heat transfer, thus a complete energy balance could not be determined for the cascade. The measured distribution of surface temperature at 0.45 and 5.9%, as shown in Fig. 12, was used as temperature boundary conditions. Linear interpolation was used between these two levels to determine the temperature boundary conditions at 2.2% turbulence intensity.

An example of the prediction of the variation of local heat transfer coefficient over the surface of the blade is presented in Fig. 13 for varying inlet turbulence intensities. As mentioned earlier the stagnation point is situated on the pressure surface, this is illustrated by the maximum heat transfer rates in this region which is offset toward the concave surface. The levels of heat transfer are in good agreement with the experimental data in the stagnation point region. No sudden transition from a purely laminar to a purely turbulent flow is observed, and this trend is well predicted by the program. At an inlet turbulence intensity level of 5.9% the predictions show some form of transition of the boundary. Although this is not in complete agreement with the experimental data, this could be due to the mixing augmentation on the concave surface dominating the favorable pressure gradient. It is well established that in a two-dimensional boundary layer, flow over a convex surface damps mixing, while a concave surface leads to augmentation as described by Bradshaw (ref. 25). On the pressure surface the prediction of the increase in the average heat transfer coefficients for increasing turbulence levels is very good. This is surprising, considering that a constant turbulent Prandtl number (=0.9) was used for these calcuations. The average gas-to-wall temperature difference was 30$^0$C; however, the gas-to-wall temperature ratio ($T_{gas}/T_{wall} \approx 1.09$) was representative of those found in the uncooled turbine stages of a gas turbine engine.

For the suction surface, a sharp increase in heat transfer between 80% and 90% chord is apparent for the low turbulence levels, and the increase is between 50% and 90% for the high turbulence level case. Fig. 11 indicates that on this surface a favorable pressure gradient, decreasing in magnitude, extends 60% of the chord downstream of the leading edge. The boundary layer then experiences an adverse pressure gradient and the high heat transfer rates in this region are indicative of transition from laminar to turbulent flow. For the 0.45% and 2.2% test cases the transition process was experimentally determined to be abrupt, which the LRN turbulence model is not able to accurately simulate. Once again the model, although only for low turbulence levels, has tended to smear the transition process over a longer distance and the onset of transition is predicted to occur too close to the leading edge. The experimental data showed little or no effect for increasing turbulence levels from 0.45% to 2.2% over the front 70% chord of the suction surface. A further increase in turbulence to 5.9% produced a significant increase in heat transfer. The length of transition of the boundary layer for this case is longer than the low freestream turbulence intensity test cases. The transition process is adequately predicted for this high turbulence level case, which is the one of the strong points of the LRN k-$\epsilon$ turbulence model. The prediction showed an increase in heat transfer from 0.45% to 2.2% which is not in agreement with the experimental data. This could be due to the interpolated blade surface temperature that was used as the boundary conditions for the 2.2% turbulence case. The actual blade surface temperature, which was not documented, could be different from that used. This could explain the discrepancy between these results.

### Flow in a Turbine End Wall Cascade

The final three-dimensional flow test case considered is secondary flow and losses in a turbine cascade. Gregory-Smith and Graves (ref. 26) investigated the flow in a cascade of large scale rotor blades of some 110 degrees of turning. The flow was traversed with 3-hole and 5-hole cobra type pressure probes. Hot-wire anemometry measurements were also carried out in the linear cascade consisting of blades scaled from the midspan section of a high-pressure turbine rotor design. The main geometric parameters for the cascade are given in Table 1. The blade profile coordinates were obtained from Gregory-Smith (ref. 27).

Table 1 Cascade Geometric Parameters

| | |
|---|---|
| Inlet flow angle | 42.75 deg. |
| Inlet blade angle | 52.25 deg. |
| Exit flow angle | -66.60 deg. |
| Exit blade angle | -67.50 deg. |
| Blade chord | 216 mm |
| Blade axial chord | 175 mm |
| Span | 457 mm |
| Pitch | 191 mm |
| Reynolds number (based on chord and exit velocity) | $5 \times 10^5$ |

The estimated inlet (99%) boundary layer thickness was 102.0 mm, the displacement thickness was 12.1 mm and the momentum thickness was 9.9 mm. These data were obtained at the first slot which was 14% of an axial chord upstream of the cascade. The measured inlet free-stream turbulence intensity was 1.4% which was due to the honeycomb flow straightener placed upstream of the cascade. The inlet boundary layer profile agrees well with a 0.12 power law profile. This profile was used for the input velocity distribution during the computational analysis.

The three-dimensional "H" grid was generated from a two-dimensional blade-to-blade grid which was projected in the spanwise direction. Grid clustering was used at the endwalls, at the blade sufaces and around the leading edge and trailing edge of profile. In the cross-plane, 31 x 31 grid points were used with 81 in the streamwise direction. A three-dimensional view of the grid is presented in Figure 14. Although the problem is symmetrical about the mid-span plane, the computation was performed for the complete cascade to check the code's ability to compute a symmetric solution.

The three-dimensional flowfield was initialised with the solution of the two-dimensional flow through the cascade. The two-dimensional version of the code was run to 500 iterations, giving two orders of magnitude convergence. The velocity field showed most of the correct features of two-dimensional flow through a cascade. As the LRN turbulence model was used (on this coarse grid) the boundary layer growth is most probably too rapid; however, this was considered to be a good initial guess for the three-dimensional flow.

The velocity field was scaled in the spanwise direction according to the inlet boundary layer profile at the endwalls. The pressure distribution was assumed constant in the spanwise direction. Less than one order of magnitude convergence was obtained for this case, which took 4000 CPU seconds on the ETA-10 at the John von Neumann Computer Center. Because of limited computation time the solution was not continued further.

The main objective of this test case is to attempt to qualitatively predict the three-dimensional viscous phenomena inside a turbine blade passage.

Fig. 15 shows the velocity vector plot for the end wall region. Flow reversal occurs at the leading edge which is associated with the roll-up of the inlet boundary layer at the leading into the so-called horse-shoe vortex. The subsequent movement of this vortex is not captured as the secondary flow convects the pressure side vortex over to the suction surface of the adjacent blade too rapidly.

The horse-shoe vortex and passage vortex begin in the leading region close to the endwall. An "H" grid does not allow the adequate resolution of the severe flow gradients in this region. This region should be resolved with a "C" grid which is continuous around the leading edge. A higher order turbulence model needs to be considered if the finer details of this complex flow is to be adequately resolved.

## CONCLUSIONS

Various test cases have been presented. These show that in two dimensions the pressure substitution method is superior to the pressure correction method. This method is ideally suited for the computation of incompressible flows.

For complex flow situations such as turbulent flow through a compressor or turbine cascade, the code exhibits satisfactory convergence behavior. The global parameters such as pressure distribution, lift coefficient and heat transfer are well predicted within engineering accuracy. The agreement between the computed and measured blade surface skin friction coefficients and heat transfer coefficients is very good. Details of the leading edge flow and particularly the trailing edge separation have been resolved, which shed more light on these complex flow regions.

For flow over curved surfaces with large pressure gradients the minimum turbulence model that must be used is the low-Reynolds number $k-\epsilon$ model. Its ability to predict transition dependent on freestream turbulence intensity is well known, and it was used in the present study to predict separated flow and flow through a turbine nozzle including heat transfer.

Experimental investigations of turbulent flow through cascades should include detailed measurements of the inlet freestream turbulence intensity and turbulence length scales. These two parameters are of vital importance for the correct specification of the inlet boundary conditions.

The three-dimensional turbulent flow through a turbine end wall cascade has been qualitatively resolved. To increase the accuracy of the predictions it is recommended that a higher order turbulence model be used which can simulate the laminar flow leading edge region.

## ACKNOWLEDGEMENTS

The authors wish to acknowledge the John von Neumann Supercomputer Center for providing computational time under grant NAC 817, and for partial support from the National Aeronautics and Space Administration through grant NSG 3266 with P. Sockol as the grant monitor.

## REFERENCES

1. Hah, C., "A Navier-Stokes Analysis of Three-Dimensional Turbulent Flows Inside Turbine Blade Rows at Design and Off-Design Conditions," *ASME J. Eng. for Power*, Vol. 106, pp. 421-429, (1984).
2. Leonard, B. P., "A Stable and Accurate Convective Modelling Procedure Based on Quadratic Upstream Interpolation," *Computer Methods in Applied Mechanics and Engineering*, Vol. 19, pp. 59-98, (1979).
3. Raithby, G. D., "Skew Upstream Differencing Schemes for Problems Invloving Fluid Flow," *Computer Methods in Applied Mechanics and Engineering*, Vol. 9, pp. 153-164, (1976).
4. Patankar, S. V., "Recent Developments in Computational Heat Transfer," *Journal of Heat Transfer*, Vol. 110, pp. 1037-1045, (1988).
5. Patel, M. K. and Markatos, N. C., "An Evaluation of Eight Discretization Schemes for Two-Dimensional Convection-Diffusion Equations," *International Journal for Numerical Methods in Fluids*, Vol. 6, pp. 129-154, (1986).
6. Patel, M. K., Cross, M., Markatos, N. C. and Mace, A. C. H., "An Evaluation of Eleven Discretization Schemes for Predicting Elliptic Flow and Heat Transfer in Supersonic Jets," *International Journal of Heat and Mass Transfer*, Vol. 30, pp. 1907-1925, (1986).
7. Rhie, C. M. and Chow, W. L., "Numerical Study of the Turbulent Flow Past an Airfoil with Trailing Edge Separation," *AIAA Journal*, Vol. 21, pp. 1525-1532, (1983).
8. Rhie, C., "A Pressure Based Navier-Stokes Solver Using the Multigrid Method," AIAA Paper 86-0207, AIAA 24th Aerospace Sciences Meeting, Reno, NV, (1986).
9. Shih, T. M. and Ren, A. L., "Primitive-Variable Formulations Using Nonstaggered Grids," *Numerical Heat Transfer*, Vol. 7, pp. 413-428, (1984).
10. Hobson, G. V. and Lakshminarayana, B., "Fully Elliptic Incompressible Flow Calculations on Regular Grid by a New Pressure Substitution Method," AIAA paper 90-0239, AIAA 28th Aerospace Sciences Meeting, Reno, NV, (1990).
11. Lam, C. K. G. and Bremhorst, K., "A Modified Form of the k-$\epsilon$ Model for Predicting Wall Turbulence," *Journal of Fluids Eng.*, Vol. 103, pp. 456-460, (1981).
12. Rhie, C., "A Three-Dimensional Passage Flow Analysis Method Aimed at Centrifugal Impellers," *Computers and Fluids*, Vol. 13, No. 4, pp. 443-460, (1985).
13. Boussinesq, J., "Theorie de l'ecoulement tourbillant," Memoires Presentes par Divers Savants Sciences Mathematique at Physiques, Academie des Sciences, Paris, France, Vol. 23, p. 46, (1877).
14. Launder, B. E. and Spalding, D. B., "The Numerical Computation of Turbulent Flows," *Computer Methods in Applied Mechanics and Engineering*, pp. 269-289, (1974).
15. Patel, V.C., Rodi, W. and Scheuerer, G., "A Review and Evaluation of Turbulence Models for Near Wall and Low Reynolds Number Flows," *AIAA Journal*, Vol. 23, pp. 1308-1319, (1985).
16. Rodi, W. and Scheuerer, G., "Calculation of Heat Transfer to

Convection-Cooled Gas Turbine Blades," *Journal of Eng. for Power*, Vol. 107, pp. 620-627, (1985).
17. Spalding, D. B., "A Novel Finite Difference Formulation for Differential Expressions Involving Both First and Second Derivatives," *Int. Journal for Numerical Methods in Engineering*, Vol. 4, pp. 551-559, (1972).
18. Napolitano, M., "A Fortran Subroutine for the Solution of Periodic Block-Tridiagonal Systems," Communications in Applied Numerical Methods, Vol. 1, pp. 11-15, (1985).
19. Thomas, L. H., "Elliptic Problems in Linear Difference Equations over a Network," Watson Sci. Comput. Lab. Rept., Columbia University, New York, (1949).
20. Rosenfeld, M. and Wolfshtein, M., "Numerical Calculations of a Laminar Two Dimensional Straight Cascade Flow," *Computer and Fluids*, Vol. 12, pp. 293-310, (1984).
21. Zierke, W. C. and Deutsch, S., "The Measurement of Boundary Layers on a Compressor Blade in Cascade: Part 4-Flow Fields for Incidence Angles of -1.5 and -8.5 Degrees," ASME 89-GT-72 (To be published in the *J. Turbomachinery*)
22. Turner, A. B., "Local Heat Transfer Measurements on a Gas Turbine Blade," *J. Mechanical Engineering Science*, Vol. 13, No. 1, (1971).
23. Bayley, F. J. and Turner, A. B., "The Heat Transfer Performance of Porous Gas Turbine Blades," *The Aeronaut. J. R. Aeronautical Soc.* 72, (1968).
24. Bayley, F. J. and Wood, G. R., "Aerodynamic Performance of Porous Gas Turbine Blades," *The Aeronautical Journal of the Royal Aeronautical Society*, Vol. 73, pp. 789-796, (1969).
25. Bradshaw, P., "Effects of Streamline Curvature on Turbulent Flow," Agardograph No. 169, (1973).
26. Gregory-Smith, D. G. and Graves, C. P., "Secondary Flows and Losses in a Turbine Cascade," AGARD Conference Proceedings No. 351, Viscous Effects in Turbomachines, (1983).
27. Gregory-Smith, D. G., Private Communications, (1989).

## APPENDIX A

Partial derivatives of any function are transformed according to,

$$\begin{aligned}\frac{\partial}{\partial x} &= \xi_x \frac{\partial}{\partial \xi} + \eta_x \frac{\partial}{\partial \eta} + \varsigma_x \frac{\partial}{\partial \varsigma} \\ \frac{\partial}{\partial y} &= \xi_y \frac{\partial}{\partial \xi} + \eta_y \frac{\partial}{\partial \eta} + \varsigma_y \frac{\partial}{\partial \varsigma} \\ \frac{\partial}{\partial z} &= \xi_z \frac{\partial}{\partial \xi} + \eta_z \frac{\partial}{\partial \eta} + \varsigma_z \frac{\partial}{\partial \varsigma}\end{aligned} \qquad [A1]$$

where,

$$
\begin{aligned}
\xi_x &= (y_\eta z_\zeta - y_\zeta z_\eta)/\mathbb{J}\\
\xi_y &= -(x_\eta z_\zeta - x_\zeta z_\eta)/\mathbb{J}\\
\xi_z &= (x_\eta y_\zeta - x_\zeta y_\eta)/\mathbb{J}\\
\eta_x &= -(y_\xi z_\zeta - y_\zeta z_\xi)/\mathbb{J}\\
\eta_y &= (x_\xi z_\zeta - x_\zeta z_\xi)/\mathbb{J}\\
\eta_z &= -(x_\xi y_\zeta - x_\zeta y_\xi)/\mathbb{J}\\
\zeta_x &= (y_\xi z_\eta - y_\eta z_\xi)/\mathbb{J}\\
\zeta_y &= -(x_\xi z_\eta - x_\eta z_\xi)/\mathbb{J}\\
\zeta_z &= (x_\xi y_\eta - x_\eta y_\xi)/\mathbb{J}
\end{aligned}
\qquad [A2]
$$

and,

$$
\mathbb{J} = \begin{vmatrix} x_\xi & x_\eta & x_\zeta \\ y_\xi & y_\eta & y_\zeta \\ z_\xi & z_\eta & z_\zeta \end{vmatrix} \qquad [A3]
$$

which is the Jacobian of the transformation.

The contravariant velocities are defined as,

$$
\begin{aligned}
G_1 &= \xi_x u + \xi_y v + \xi_z w\\
G_2 &= \eta_x u + \eta_y v + \eta_z w\\
G_3 &= \zeta_x u + \zeta_y v + \zeta_z w
\end{aligned}
\qquad [A4]
$$

and the additional transformation metrics as,

$$
\begin{aligned}
\alpha &= \xi_x^2 + \xi_y^2 + \xi_z^2\\
\beta &= \eta_x^2 + \eta_y^2 + \eta_z^2\\
\gamma &= \zeta_x^2 + \zeta_y^2 + \zeta_z^2
\end{aligned}
\qquad [A5]
$$

and,

$$
\begin{aligned}
H_1 &= \xi_x \eta_x + \xi_y \eta_y + \xi_z \eta_z\\
H_2 &= \xi_x \zeta_x + \xi_y \zeta_y + \xi_z \zeta_z\\
H_3 &= \eta_x \zeta_x + \eta_y \zeta_y + \eta_z \zeta_z
\end{aligned}
\qquad [A6]
$$

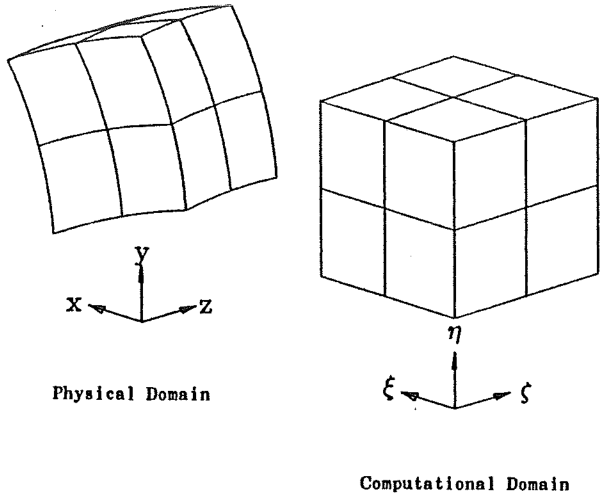

Fig. 1 Transformation Representation

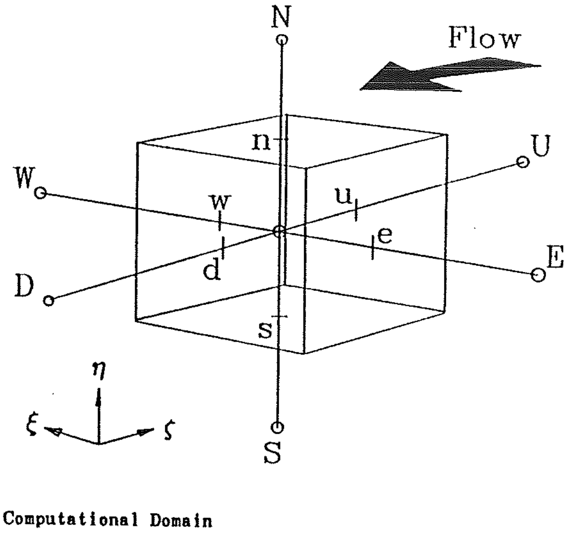

Fig. 2 Control Volume

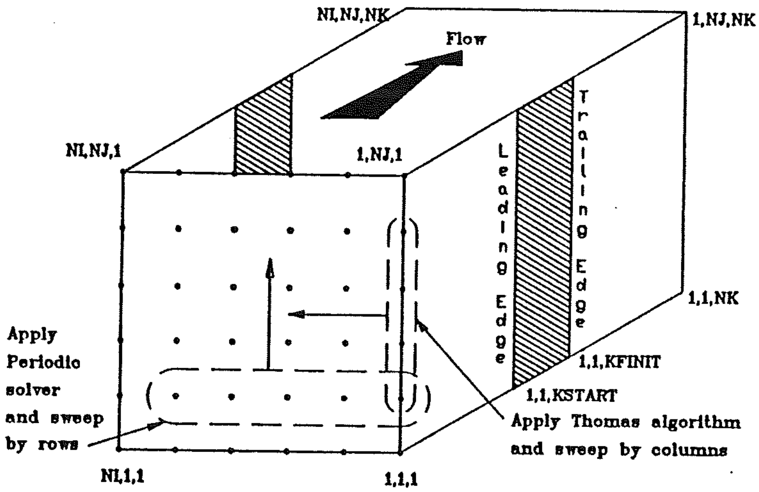

Fig. 3 Alternating Direction Implicit Relaxation of a Three-Dimensional Cascade Geometry

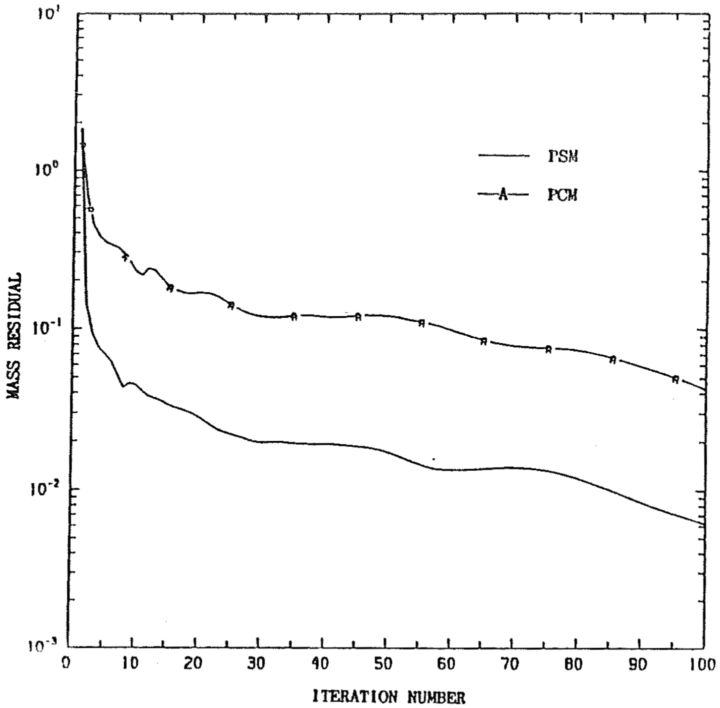

Fig. 4 Comparison of Convergence Rates for PSM and PCM; Laminar Flow in a Cascade, $\omega_u = \omega_v = 0.8$, $\omega_p = 1.0$

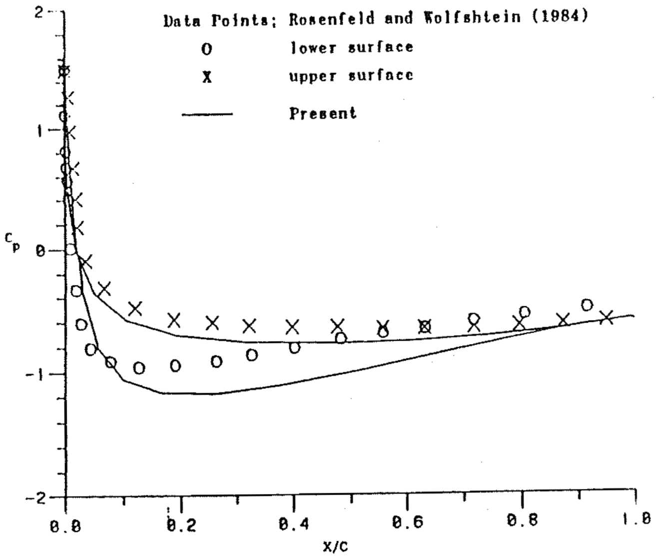

Fig. 5 Comparison of Predicted Pressure Coefficient for a Straight Cascade of NACA 0012 Blade Profiles at 30 Deg. Stagger and 0.0 Deg. Incidence

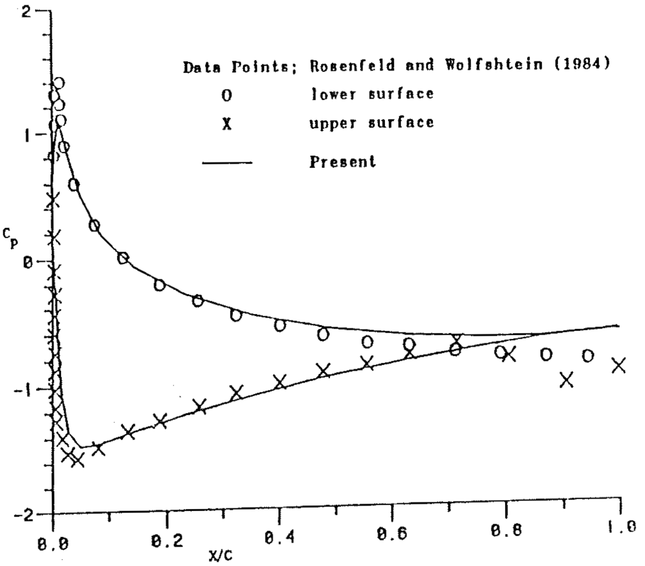

Fig. 6 Comparison of Predicted Pressure Coefficient for a Straight Cascade of NACA 0012 Blade Pr at 30 Deg. Stagger and -10.0 Deg. Incidence

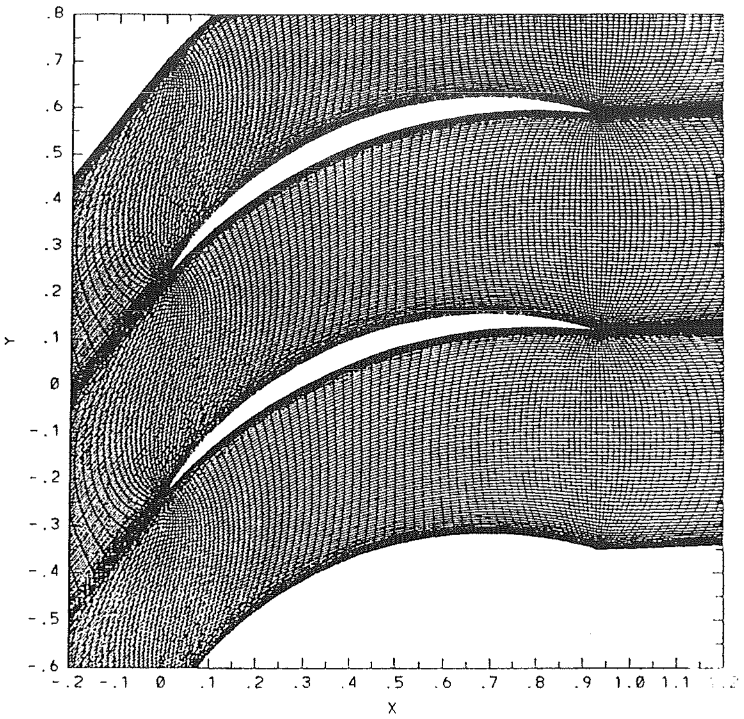

Fig. 7 Computational Grid for the Double Circular Arc Cascade

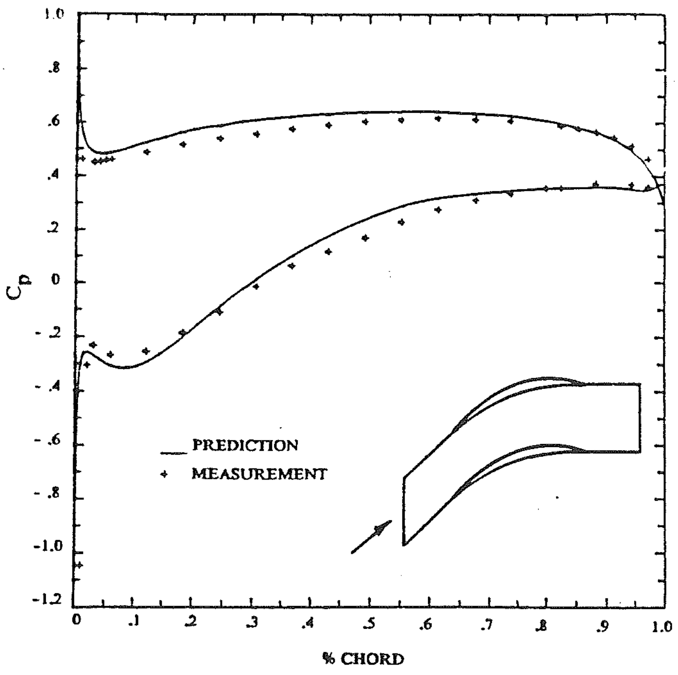

Fig. 8 Comparison between Experimental and Computed Static Pressure Coefficient for DCA Cascade

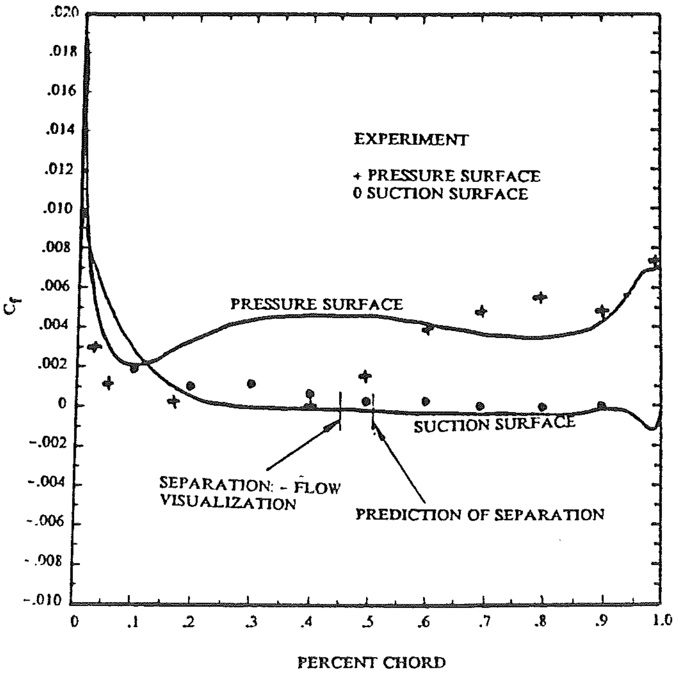

Fig. 9 Comparison of the Computed and Measured Skin Friction Coefficient on the Blade Surface

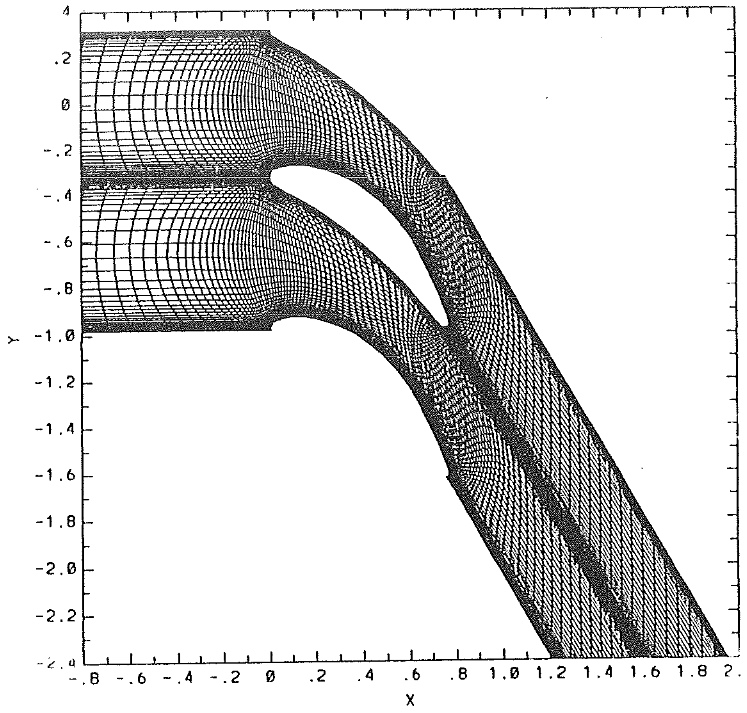

Fig. 10 Computational Grid for the Turbine Nozzle Cascade

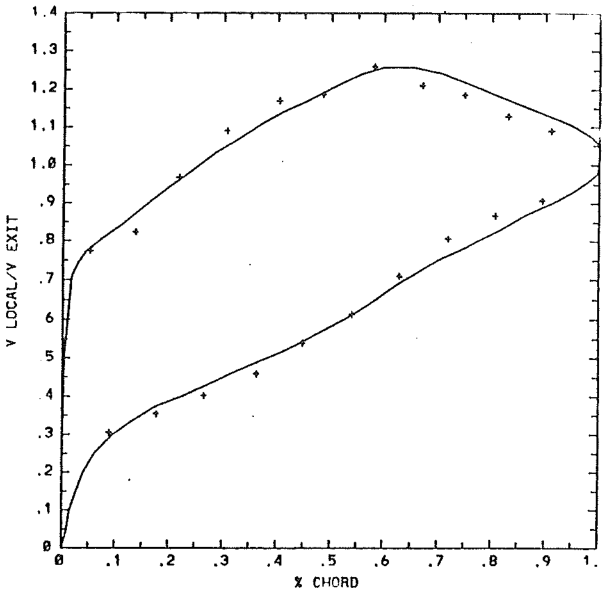

Fig. 11 Comparison of the Predicted and Measured Local Velocity Distribution for the Turbine Nozzle

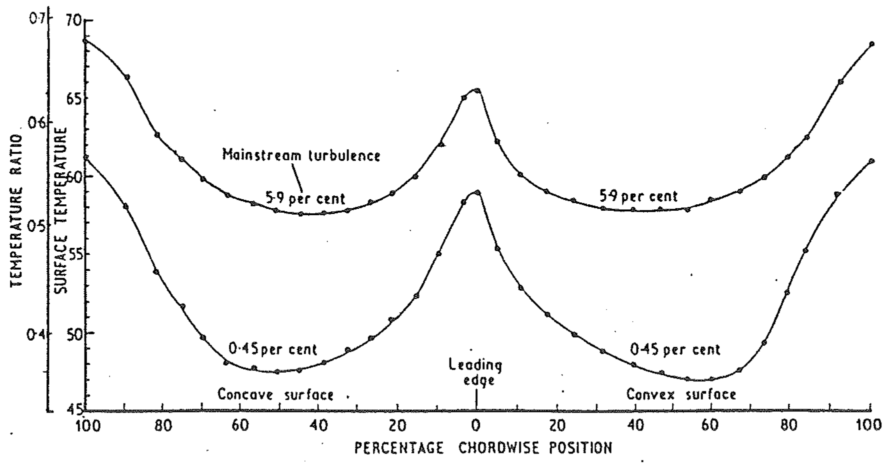

Fig. 12 Measured Blade Surface Temperature Distribution: Turner (ref. 22)

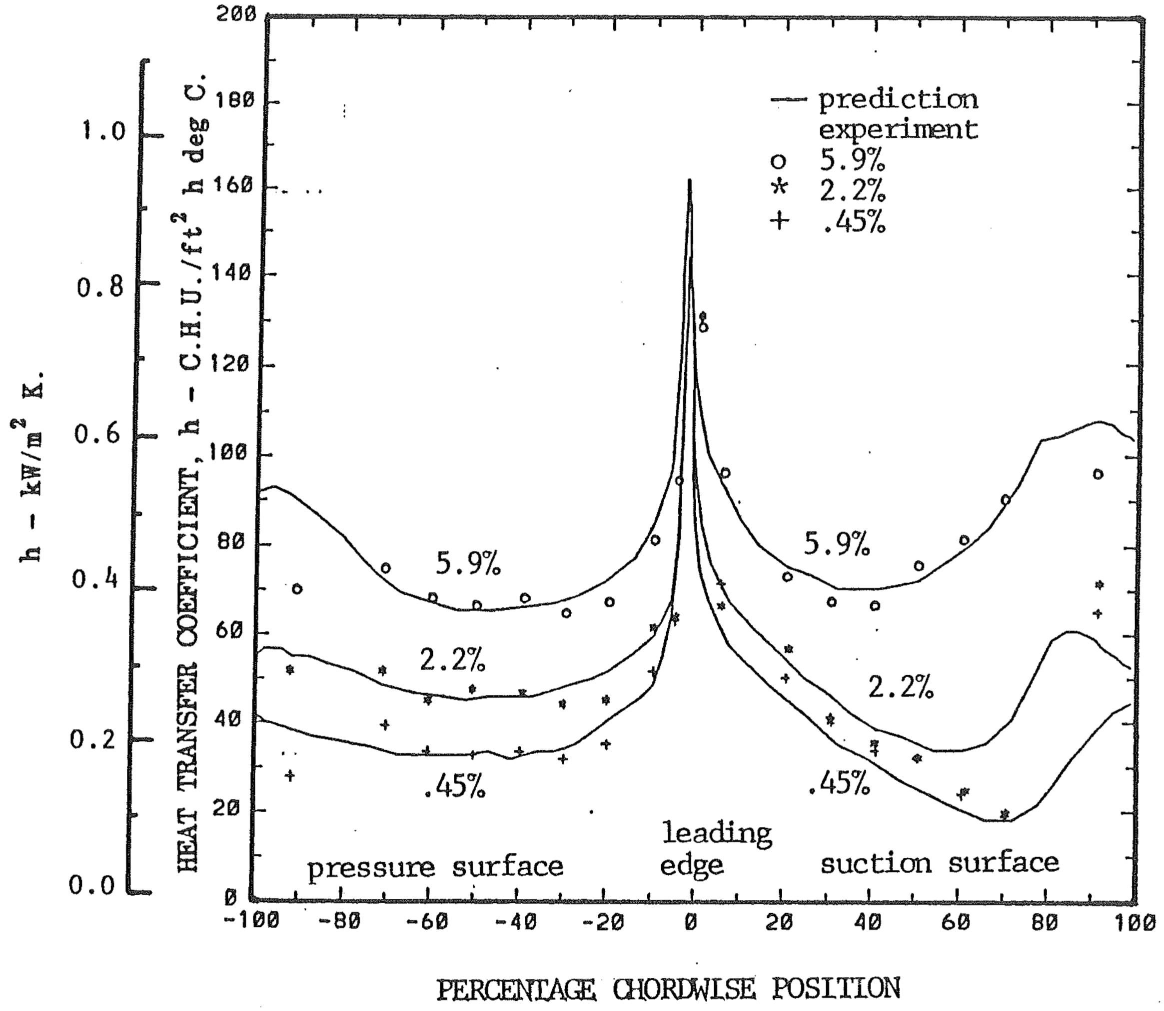

Fig. 13 Comparison of Experimental and Predicted Distribution of Heat Transfer Coefficient with Varying Inlet Freestream Turbulence Intensities

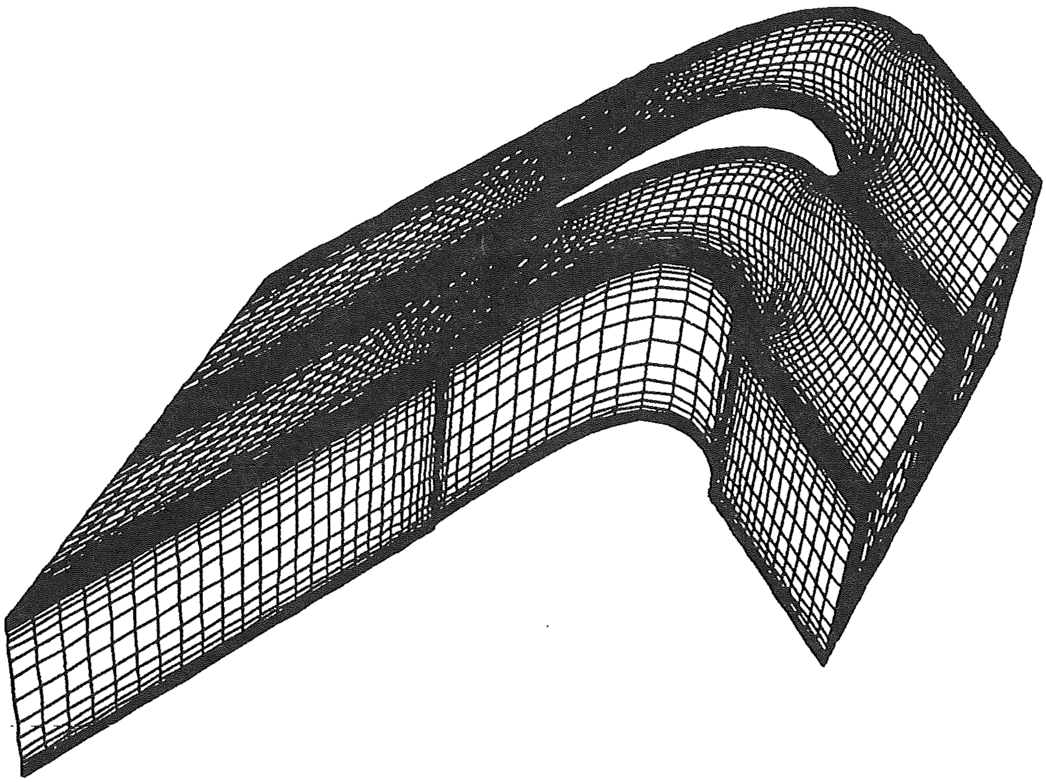

Fig. 14 Computational Grid for the Turbine End Wall Cascade

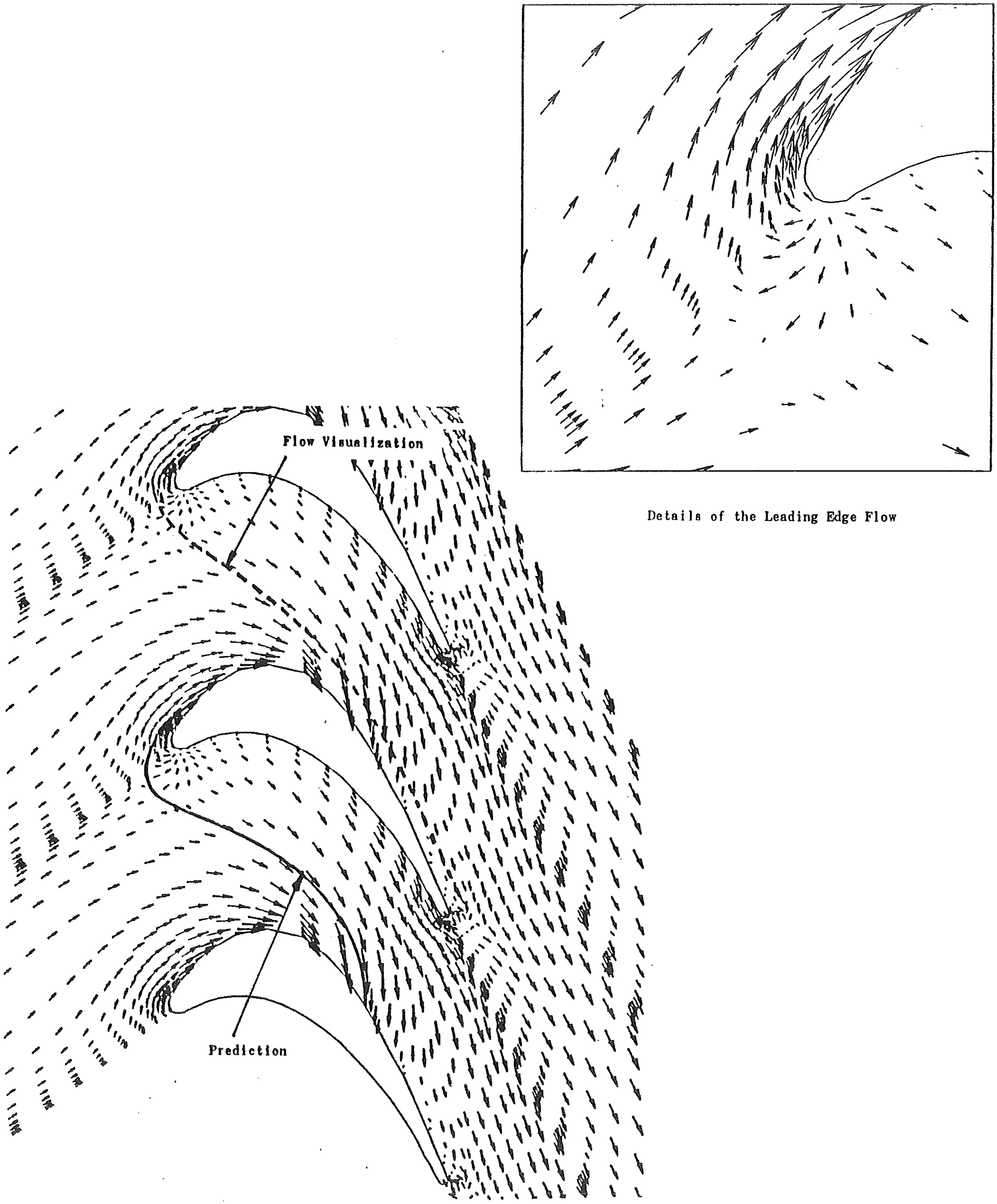

Details of the Leading Edge Flow

Fig. 15 End-Wall Velocity Vector Plot Showing the Development of the Horse Vortex System